Image quality of microcalcifications in digital breast tomosynthesis: Effects of projection-view distributions

Yao Lu,[a] Heang-Ping Chan, Jun Wei, Mitch Goodsitt, Paul L. Carson, and Lubomir Hadjiiski
Department of Radiology, University of Michigan, Ann Arbor, Michigan 48109-5842

Andrea Schmitz, Jeffrey W. Eberhard, and Bernhard E. H. Claus
GE Global Research, Niskayuna, New York 12309

(Received 1 April 2011; revised 5 July 2011; accepted for publication 19 July 2011; published 26 September 2011)

Purpose: To analyze the effects of projection-view (PV) distribution on the contrast and spatial blurring of microcalcifications on the tomosynthesized slices (X-Y plane) and along the depth (Z) direction for the same radiation dose in digital breast tomosynthesis (DBT).
Methods: A GE GEN2 prototype DBT system was used for acquisition of DBT scans. The system acquires PV images from 21 angles in 3° increments over a ±30° range. From these acquired PV images, the authors selected six subsets of PV images to simulate DBT of different angular ranges and angular increments. The number of PV images in each subset was fixed at 11 to simulate a constant total dose. These different PV distributions were subjectively divided into three categories: uniform group, nonuniform central group, and nonuniform extreme group with different angular ranges and angular increments. The simultaneous algebraic reconstruction technique (SART) was applied to each subset to reconstruct the DBT slices. A selective diffusion regularization method was employed to suppress noise. The image quality of microcalcifications in the reconstructed DBTs with different PV distributions was compared using the DBT scans of an American College of Radiology phantom and three human subjects. The contrast-to-noise ratio (CNR) and the full width at half maximum (FWHM) of the line profiles of microcalcifications within their in-focus DBT slices (parallel to detector plane) and the FWHMs of the interplane artifact spread function (ASF) in the Z-direction (perpendicular to detector plane) were used as image quality measures.
Results: The results indicate that DBT acquired with a large angular range or, for an equal angular range,with a large fraction of PVs at large angles yielded superior ASF with smaller FWHM in the Z-direction. PV distributions with a narrow angular range or a large fraction of PVs at small angles had stronger interplane artifacts. In the X-Y focal planes, the effect of PV distributions on spatial blurring depended on the directions. In the X-direction (perpendicular to the chestwall), the normalized line profiles of the calcifications reconstructed with the different PV distributions were similar in terms of FWHM; the differences in the FWHMs between the different PV distributions were less than half a pixel. In the Y-direction (x-ray source motion), the normalized line profiles of the calcifications reconstructed with PVs acquired with a narrow angular range or a large fraction of PVs at small angles had smaller FWHMs and thus less blurring of the line profiles. In addition, PV distributions with a narrow angular range or a large fraction of PVs at small angles yielded slightly higher CNR than those with a wide angular range for small, subtle microcalcifications; however, PV distributions had no obvious effect on CNR for relatively large microcalcifications.
Conclusions: PV distributions affect the image quality of DBT. The relative importance of the impact depends on the characteristics of the signal and the direction (perpendicular or parallel) relative to the direction of x-ray source motion. For a given number of PVs, the angular range and the distribution of the PVs affect the degree of in-plane and interplane blurring in opposite ways. The design of the scan parameters of tomosynthesis systems would require proper consideration of the characteristics of the signals of interest and the potential trade-off of the image quality of different types of signals. [DOI: 10.1118/1.3637492]

Key words: breast tomosynthesis, projection-view distribution, microcalcifications, image quality

I. INTRODUCTION

Digital breast tomosynthesis (DBT) is an emerging imaging modality that utilizes limited-angle tomography technology to provide quasi-three-dimensional (3D) structural information of the breast. Low-dose x-ray projections of the breast are acquired at a small number of angles over a limited angular range.[1,2] The total radiation dose of a DBT scan can be set to be comparable to that of a single mammogram. A set of tomosynthesized slices is reconstructed from the limited-angle projections. DBT builds on the advantages of current full field digital mammography (FFDM) technology, extending it to include 3D information of anatomical structures,

thus alleviating to some extent the limitation of FFDM in detecting cancerous lesions in dense breasts. The spatial resolution of the reconstructed images (slices) approaches that of the detector while the resolution in the depth direction is poor due to the missing information over the angular space that is not sampled.

DBT offers strong potential to improve mass detection compared to FFDM.[3–5] The detection of microcalcifications is more sensitive to the reconstruction image quality because of the small size and low contrast of subtle microcalcifications. The reconstructed image quality is affected by many factors, including those related to the DBT system design and the reconstruction techniques. Understanding of the dependence of image quality on these factors will be useful for the optimization of DBT for various applications.

Optimization of system parameters has been studied with different tomosynthesis systems and various reconstruction techniques. Pineda *et al.*[6] used a mathematical observer model to optimize a chest tomosynthesis system. Li *et al.*[7] analyzed the slice sensitivity profile (SSP) as a function of projection angles and applied it to optimize a radiographic tomosynthesis system. Hu *et al.*[8] employed a linear system model to optimize the modulation transfer function (MTF) of DBT reconstructed with filtered back projection (FBP). Zhang *et al.*[9] investigated the effects of projection-view (PV) distribution on the artifact spread function (ASF) and contrast-to-noise ratio (CNR) of simulated masses and high-density objects in DBT reconstructed with the simultaneous algebraic reconstruction technique (SART). Ren *et al.*[10] investigated the relationship between CNR and FBP-type reconstruction methods in a DBT system optimization study. Chawla *et al.*[11] evaluated lesion detectability in FBP-reconstructed chest tomosynthesis images and studied its dependence on image acquisition parameters using a Laguerre-Gauss channelized Hotelling observer model. Sechopoulos *et al.*[12] investigated a large combination of angular ranges and number of projections using a computer simulation model of DBT systems and iterative maximum-likelihood expectation-maximization (MLEM) approach. Reiser *et al.*[13] used an observer model to investigate the effect of acquisition parameters and quantum noise on DBT reconstructed with an iterative MLEM method. Nishikawa *et al.*[14] proposed to apply variable dose for different PVs in DBT, and among those projections, one high dose projection would be used for microcalcification detection and the MLEM reconstructed images for mass detection. The previous works used physical properties such as MTF, ASF, CNR, SSP, and mathematical observer models for optimization of DBT systems. These studies showed that, in general, decreasing acquisition angular range degraded the depth resolution,[7–10,12] and the CNR for masses was improved with increasing scan angular range,[9,12] while CNR for microcalcifications was less sensitive to the angular range compared to mass.[12] However, Ren *et al.*[10] found that the choice of filters in their FBP method dominated the effect of acquisition angular range on CNR. In addition, these performance measures of an DBT system depended on the detection tasks and signal size.[11,13]

Spatial blurring of signals in a tomosynthesis reconstructed image volume depends on the limited-angle geometry and reconstruction methods. The optimal DBT system parameters may depend on the lesion types including soft tissue lesions (mass and architectural distortion) and microcalcifications. In our previous study,[9] we investigated the effects of PV distribution on image quality of masses in DBT. Our results demonstrated that large DBT angular range yielded superior CNR and ASF for masses and less interplane blurring but inferior in-plane edge sharpness for high-density objects.[9] Image quality is also essential for the detection and diagnosis of microcalcifications. In DBT, to keep the total radiation dose of a DBT scan about the same as that of a regular mammogram, the dose for each PV of the DBT is only a small fraction of that of a mammogram.[1,2] The low radiation dose results in much noisier PV images than FFDM. Tomosynthesis reconstruction methods are sensitive to the noise in the PVs because of the ill-posed linear system arising from the limited-angle data. For iterative reconstruction methods such as SART and MLEM,[15,16] image noise is amplified as the number of iterations increases, reducing the conspicuity of subtle microcalcifications. The noisy background has a detrimental effect for both qualitative assessment and quantitative analysis of microcalcifications. We have developed a selective-diffusion (SD) regularization method for SART to enhance microcalcifications in DBT.[17] The SD regularization method incorporates image analysis into the iterative reconstruction process to differentiate potential microcalcifications from noisy background. Different degrees of regularization are selectively applied to the potential signals and noisy background during iterative reconstruction. SART with SD regularization will suppress noise and reduce the effect of noise on both the CNR and spatial blurring of microcalcifications.

The aim of this study was to analyze the effect of PV distributions on image quality, including the CNR and spatial blurring on the tomosynthesized slices (X-Y plane) and along the depth (Z) direction, of microcalcifications in DBT. Several subsets of PVs were selected from the original DBT scan to simulate DBT distributions of different angular ranges and angular increments, under the constraint of fixed total dose. SART with SD regularization and the same reconstruction parameters was used for DBT reconstruction. We compared the CNR and image blurring of microcalcifications reconstructed from the different PV distributions. This study will provide useful information on the design of DBT systems for detection of microcalcifications.

II. MATERIALS AND METHODS

II.A. Breast tomosynthesis system

A General Electric (GE) GEN2 DBT system at the University of Michigan was used to acquire DBT scans in this study. The imaging geometry of this DBT system is illustrated in Fig. 1. The distance from x-ray focal spot to the fulcrum of the rotation is 64 cm, and the

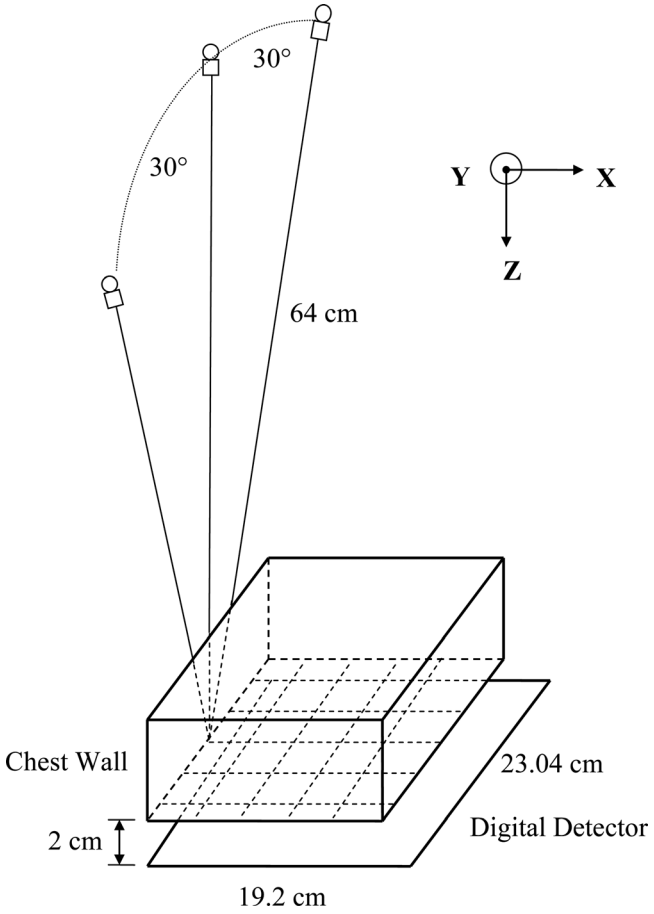

FIG. 1. Geometry of the GE prototype GEN2 digital breast tomosynthesis system used in this study. In our DBT reconstruction, the coordinate system is oriented such that the X-direction was perpendicular to the x-ray source motion direction, the Y-direction was parallel to the x-ray source motion direction, the X-Y plane was parallel to the detector plane, and the Z-direction was perpendicular to the detector plane.

x-ray source rotation plane is parallel to the chest wall and perpendicular to the detector plane. The system has a CsI phosphor/a:Si active matrix flat panel digital detector with a matrix size of 1920×2304 pixels and a pixel pitch of $0.1\,\text{mm} \times 0.1\,\text{mm}$. The digital detector is stationary during image acquisition. The system uses a step-and-shoot design and acquires PV images from a total of 21 angles in 3° increments over a $\pm 30°$ range in less than 8 s. The DBT system uses an Rh-target/Rh-filter x-ray source for all breast thicknesses.

We acquired DBT scans of an American College of Radiology (ACR) mammography phantom and human subjects with biopsy-proven calcifications for data analysis. Patient imaging was performed with IRB approval and written informed consent. The DBT scans of three subjects with malignant clusters containing microcalcifications of various sizes and contrasts were chosen as examples in this study. For the ACR phantom, the images were acquired with an exposure technique of 29 kV and a total of 95.6 mAs for 21 PVs. The mean glandular dose of the ACR phantom was estimated to be 2.5 mGy. Phantom imaging was repeated six times under the same imaging conditions. The phantom was repositioned and recompressed to a similar force for each repeated scan. The breast thickness of the three subjects ranged from 5.67 to 7.80 cm. The DBT scans were acquired with 29 to 33 kV and a total mAs of 134 to 149 for the 21 PVs.

In our reconstruction algorithm, the voxel resolution of the imaged volume in the X and Y directions were both chosen to be 0.1 mm, the same as the pixel pitch of the detector. The slice spacing in the Z direction was chosen to be 1 mm. In our study, a ray-tracing algorithm similar to the Siddon algorithm is employed for calculating the contribution of each voxel to the forward projection.[18] Logarithmic transformation is applied to the raw pixel intensities of the detected image before reconstruction. The projection model assumes a monoenergetic x-ray source and ignores the effects of scattering and beam hardening, similar to the approach by Wu *et al.*[2,15]

II.B. DBT reconstruction

SART was used for DBT reconstruction in this study. SART is an iterative algorithm which has fast convergence speed. The linear attenuation coefficient of each voxel is updated after all rays in one PV have been processed once. The number of updates in one SART iteration is equal to the number of PVs. SART is applicable to any imaging geometry and can be easily adapted to different physical models. The details of our implementation of the SART method have been described in the literature.[16] It has been proven that the iterated solution of SART converges to a weighted least square solution of the projection model ($\boldsymbol{Au}=\boldsymbol{f}$ where $\boldsymbol{A}$ is the projection matrix, $\boldsymbol{u}$ is the vector of linear attenuation coefficients to be estimated by reconstruction, and $\boldsymbol{f}$ is the vector of logarithm of the normalized x-ray intensity detected by the detector pixels),[19] which is not stable and is sensitive to the noise contained in the PVs due to the ill-posedness of this under-determined linear system.

Regularization is a promising approach to reducing noise in DBT reconstructions. However, most existing regularization methods that are adapted from general computed tomography (CT) applications do not properly take into consideration the potential presence of subtle lesions such as microcalcifications. Small, subtle microcalcifications that have relatively low contrast can occur anywhere within the breast. The gradient-driven regularization methods use local gradients to guide the regularization, and as a result, low-contrast signals such as small microcalcifications will be smoothed out as noise. We have recently developed a new selective-diffusion (SD) regularization method to control the noise without smoothing the microcalcifications.[17] Potential microcalcifications are differentiated from the noisy background and different degrees of regularization are applied to the signal or noise classes such that microcalcifications is preserved while noise is suppressed.

For SART with SD regularization, the voxel value of the image vector $\boldsymbol{u}^{(n)}$ is updated by

$$\boldsymbol{u}_j^{(n)} = \begin{cases} \boldsymbol{u}_j^{(n-1)} + \dfrac{\lambda}{\boldsymbol{A}_{+j,n}} \left(\displaystyle\sum_{i=1}^{I} \frac{\boldsymbol{A}_{ij,n}}{\boldsymbol{A}_{i+,n}} \left(f_{i.n} - (\boldsymbol{A}_n \boldsymbol{u}^{(n-1)}) \right)_i + a\omega \left(\nabla \cdot \left(|\nabla \boldsymbol{u}^{(n-1)}|^a \dfrac{\nabla \boldsymbol{u}^{(n-1)}}{|\nabla \boldsymbol{u}^{(n-1)}|^2} \right) \right)_j \right), & |\nabla \boldsymbol{u}_j^{(n-1)}| \geq \delta \\ \boldsymbol{u}_j^{(n-1)} + \dfrac{\lambda}{\boldsymbol{A}_{+j,n}} \left(\displaystyle\sum_{i=1}^{I} \frac{\boldsymbol{A}_{ij,n}}{\boldsymbol{A}_{i+,n}} \left(f_{i.n} - (\boldsymbol{A}_n \boldsymbol{u}^{(n-1)}) \right)_i + b\omega \left(\nabla \cdot \left(|\nabla \boldsymbol{u}^{(n-1)}|^b \dfrac{\nabla \boldsymbol{u}^{(n-1)}}{|\nabla \boldsymbol{u}^{(n-1)}|^2} \right) \right)_j \right), & |\nabla \boldsymbol{u}_j^{(n-1)}| < \delta \end{cases} \quad (1)$$

where $1 \leq i \leq I$, $1 \leq n \leq N$, $1 \leq j \leq J$, I is the number of pixels of the detector, N is the number of PVs, J is the number of voxels in the reconstructed imaged volume, $\boldsymbol{A}_{i+,n}$ and $\boldsymbol{A}_{+j,n}$ are the row sums and column sums of the projection matrix $\boldsymbol{A}_n$ for the nth PV, and λ is the relaxation parameter controlling the convergence of SART. For simplicity, the index for the iteration number is not explicitly included in Eq. (1). ∇ is the gradient operator, $|\nabla \boldsymbol{u}_j|$ is the gradient norm at the jth voxel of $\boldsymbol{u}$, ω is the regularization parameter, δ is a threshold to distinguish signals from noise, and a and b are parameters to control the degrees of regularization, $0 \leq a \ll b \leq 2$. Details of our SART reconstruction with SD regularization can be found in the literature.[17]

II.C. DBT PV distribution

To study the relationship between the PV distribution and the reconstructed image quality, we selected six subsets of PVs from the 21 acquired PV images to simulate DBT of different angular ranges and angular increments. The six PV distributions of DBT were selected following our previous study of the dependence of mass image quality on PV distribution of DBT.[9] The PV distributions are shown schematically in Fig. 2 and the angles of the PVs are listed in Table I. The number of PV images in each subset was chosen to be a constant of 11 to simulate a fixed total dose. The selected PV distributions were symmetric about the 0° PV, which had the central ray of the x-ray beam perpendicular to the detector. The six PV distributions may be roughly divided into three categories, referred to as (1) uniform group: *uniform narrow* (UN) and *uniform wide* (UW), (2) nonuniform central group: *nonuniform central dense* (NCD) and *nonuniform central sparse* (NCS), and (3) nonuniform extreme group: *nonuniform extreme dense* (NED), and *nonuniform extreme sparse* (NES). The PV distributions were selected to evaluate the trade-offs among the PV images acquired at small and large angles for a fixed radiation dose. As a reference for comparison, the full set of 21 PVs (FS) was also reconstructed and analyzed.

II.D. Figure of merit

The image quality of DBT reconstructed from the different PV distributions was evaluated quantitatively using selected image quality measures.

The normalized line profile and its full width at half maximum (FWHM) in the focal plane of a calcification were used to measure the in-plane image sharpness. The line profile was assumed to be the sum of a Gaussian function (the calcification) and a linear function (the local background). Least-squares curve fitting was used to fit the summed functions to the line profile. The fitted Gaussian function thus represented the normalized calcification profile after background subtraction. The FWHM of the calcification was computed as

$$\mathrm{FWHM} = (2\sqrt{2\ln 2})\sigma, \quad (2)$$

where σ is the standard deviation of the fitted Gaussian function.

An artifact spread function (ASF), defined as the normalized CNR as a function of distance in the Z direction from the focal plane of a calcification, z_o, and the FWHM of the ASF were used to measure the interplane blurring.[2] The CNR value is defined by

$$\mathrm{CNR}(z) = \frac{\bar{I}_{\mathrm{ROI}}(z) - \bar{I}_{\mathrm{BG}}(z)}{\sigma_{\mathrm{BG}}(z)}, \quad (3)$$

where $\bar{I}_{ROI}$ is the mean pixel value in a selected region of interest (ROI) centered at the same pixel location as the center of the calcification but at a depth z, $\bar{I}_{BG}$ is the mean pixel value in an ROI of a background region in the same depth, and σ_{BG} is the standard deviation of pixel values in the background ROI. The ASF(z-z_o) is, therefore, given by

$$\mathrm{ASF}(z - z_0) = \frac{\mathrm{CNR}(z)}{\mathrm{CNR}(z_0)} \quad (4)$$

where z-z_o is the distance from the focal plane. The FWHM of an ASF was estimated from a Gaussian function fitted to the ASF.

II.E. Study conditions

DBT images of an ACR phantom and three patient breasts were reconstructed with SART using seven PV distributions. For the DBT reconstructed from each subset of PV images, four SART iterations were performed. The full set of 21 PVs was reconstructed using two SART iterations such that the total number of reconstruction image volume updates (21×2) was about the same as those in the subset reconstructions (11×4).

The parameters used for SART with SD regularization were chosen in our previous study.[17] Specifically, the relaxation parameter λ was set to be 0.5 for the first SART iteration and 0.3 for the subsequent iterations. The regularization parameter ω was selected as 0.003, and parameters a and b were chosen to be 0 and 2, respectively, so that no regularization was applied to the class of signals, and strong regularization (quadratic Laplacian regularization[20]) was applied to the class of noise. Therefore, in the regions containing

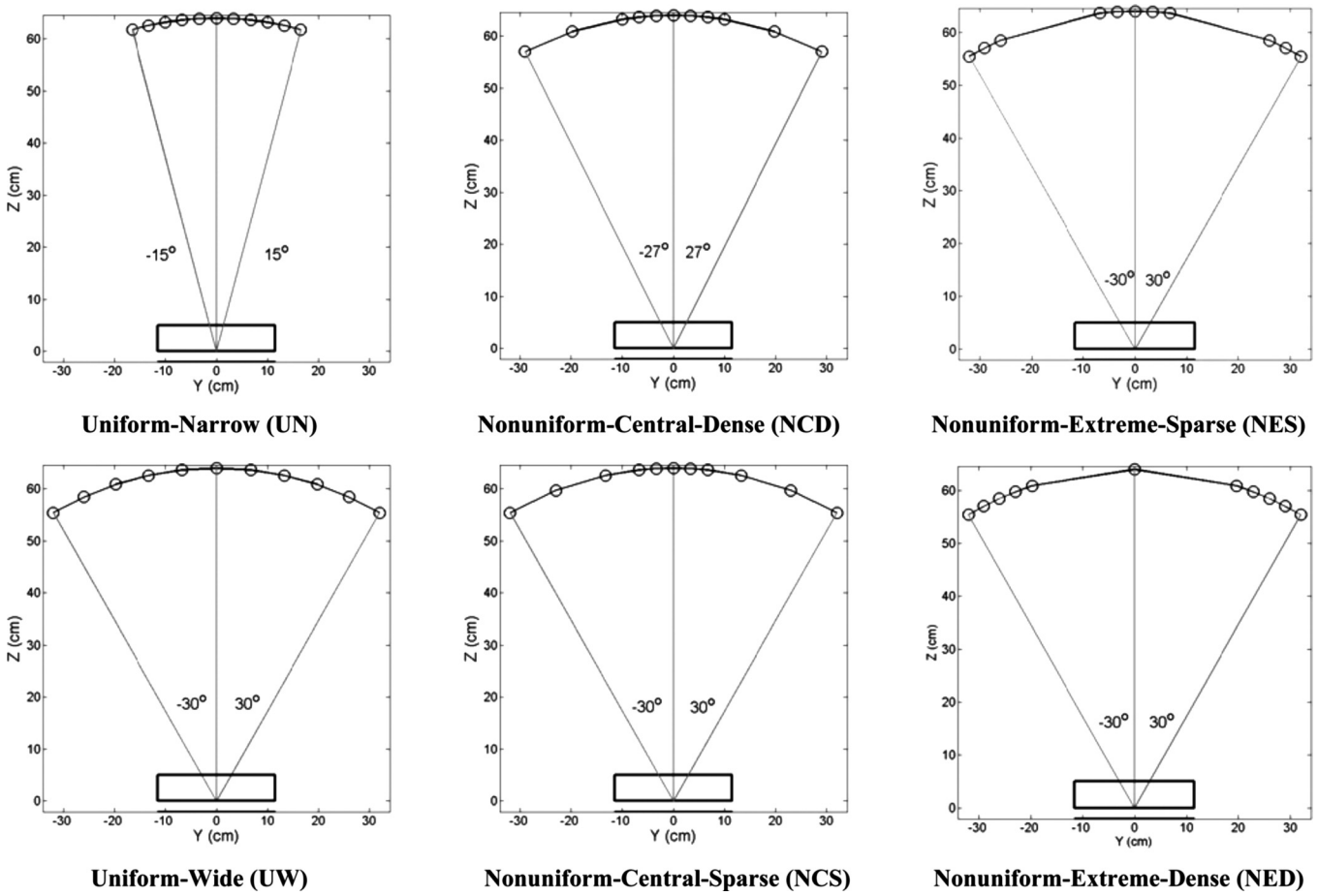

FIG. 2. Six different subsets of PV images and their distributions: (column 1) uniform group, (column 2) non-uniform central group, and (column 3) non-uniform extreme group.

potential signals, regularization would be less likely to cause image blurring, while in the background area, regularization suppressed noise and provided higher CNR and smoother baselines for curve fitting involved in the FWHM measures.

We analyzed three clusters of simulated microcalcifications from the reconstructed ACR phantom images for the quantitative analysis. The nominal diameters of the aluminum oxide specks are 0.54, 0.32, and 0.24 mm, respectively, which are smaller than the slice interval of 1 mm used in this study. For the simulated microcalcifications, all measurements were averaged over six repeated DBT scans of the same phantom under the same imaging conditions and the standard deviations were estimated. One speck was selected from each of the two groups with relatively high contrast microcalcifications (signal 1: 0.54 mm and signal 2: 0.32 mm). Five specks were selected from the group with subtle microcalcifications (signal 3: 0.24 mm) (see Fig. 3) and the image quality measures for this group were averaged over the five specks. One of the specks in the 0.24 mm group was excluded because it was visually much more subtle than the other five specks in the group both on FFDM and on the reconstructed DBT images, which indicated that its size might be an outlier compared to the other five. For signal 1 and signal 2, the six measurements of the same speck seemed to be more consistent (small standard deviations) so that averaging over the different specks in the same group was not performed.

TABLE I. Projection angles of the six PV distributions selected in this study.

PV distribution	Projection angles					
Uniform narrow (UN)	±15°	±12°	±9°	±6°	±3°	0°
Uniform wide (UW)	±30°	±24°	±18°	±12°	±6°	0°
Nonuniform central dense (NCD)	±27°	±18°	±9°	±6°	±3°	0°
Nonuniform central sparse (NCS)	±30°	±21°	±12°	±6°	±3°	0°
Nonuniform extreme sparse (NES)	±30°	±27°	±24°	±6°	±3°	0°
Nonuniform extreme dense (NED)	±30°	±27°	±24°	±21°	±18°	0°

III. RESULTS

III.A. Phantom calcifications

The CNR of the microcalcifications of three different nominal diameters reconstructed from the six PV subset distributions and the full set are shown in Fig. 4. For relatively high-contrast microcalcifications such as signal 1 and signal 2, the CNR of the six PV distributions were similar and the differences between the different PV distributions were less than 10% for signal 1 and less than 30% for signal 2. For relatively low-contrast signals such as signal 3, DBT

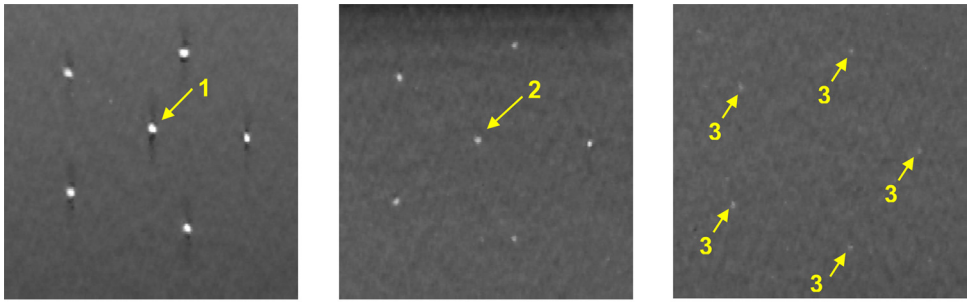

FIG. 3. Regions of interest from a DBT slice of the ACR phantom reconstructed from 21 PVs by SART with selective diffusion regularization showing (a) the first, (b) the third, and (c) the fourth speck groups with nominal speck size of 0.54, 0.32, and 0.24 mm, respectively, selected for analysis in this study.

acquired with a narrow angular range or a PV distribution that had dense sampling at the small angles such as UN and NCD yielded slightly higher CNR than the other PV distributions. The CNR from the UN distribution was about twice the CNR from the NED distribution that had dense sampling at the large angles. The standard deviations of the high-contrast signals were relatively small compared to those of the subtle signals. The CNR from the FS that had about twice as many PVs was about 40% higher than the CNR from other PV distributions, as may be expected from the two times higher dose.

In the X-Y focal plane, the image blurring depends on the direction. Figure 5(a) shows the FWHMs of the normalized line profiles in the X-direction (perpendicular to the x-ray source motion) of the three microcalcifications reconstructed from the six PV distributions and the full set. For the relatively high-contrast microcalcifications (signal 1 and signal 2), the average FWHMs of the normalized line profiles obtained from the six PV distributions were similar; the differences in the average FWHMs between the different PV distributions were less than half a pixel and the standard deviations were small. For subtle microcalcifications (signal 3), the FWHM of the normalized line profiles varied and the standard deviations were large; the variation in the average FWHMs for the different PV distributions was within one standard deviation. Figure 5(b) shows the FWHMs of the normalized line profiles in the Y-direction (parallel to the x-ray source motion) obtained from the six PV distributions and the full set. It can be observed that microcalcifications of different sizes have similar trends. DBT acquired with a narrow angular range that had dense sampling at the small angles such as UN and NCD yielded smaller FWHMs and thus less blurring in the Y-direction while DBT acquired with a large angular range such as UW and NED as well as FS had greater blurring in the Y-direction. Furthermore, NED that lack PVs in the small angles yielded the largest FWHMs and thus worst blurring in the Y-direction among all PV distributions. The large microcalcification (signal 1) had small standard deviations. For the mid-size microcalcification (signal 2), PV distributions with more PVs at large angles had larger standard deviation than PV distributions with more PVs at small angles. The subtle microcalcifications (signal 3) have large standard deviations for all PV distributions.

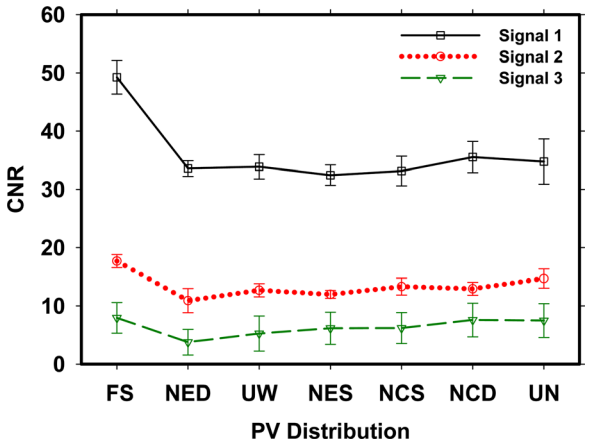

FIG. 4. Comparison of the CNR using different PV distributions. The CNR of signals presented in Fig. 3 for three clusters of simulated microcalcifications selected from the ACR phantom images reconstructed by SART with selective diffusion regularization are compared. All values of signal 1 (nominal size 0.54 mm) and signal 2 (nominal size 0.32 mm) were obtained by averaging six repeated measurements. All values of signal 3 were obtained by averaging five simulated microcalcifications in the speck group of nominal size 0.24 mm and six repeated measurements. The error bars indicate one standard deviation of the measurements. Six subsets and the full set of projection views are compared. Data points of the same signal are connected by lines to facilitate reading the graph, not to indicate functional relationships.

Figure 5(c) shows the FWHMs of the ASFs in the Z-direction (depth direction). The interplane artifacts were similar for the high-contrast microcalcifications (signal 1 and signal 2). The interplane artifacts for the PV distributions with a large angular range such as UW and NED did not extend as far as those of other PV distributions. The trends were opposite to the blurring observed from the same microcalcifications in the Y-direction. For subtle calcifications (signal 3), the FWHMs of ASF varied; the differences in their mean values among different PV distributions were less than 0.3 mm but the standard deviations were large. It may also be noted that the reconstruction slice interval was 1 mm so that the interplane blurring of subtle microcalcifications might have been masked by the coarse slice interval for any PV distributions.

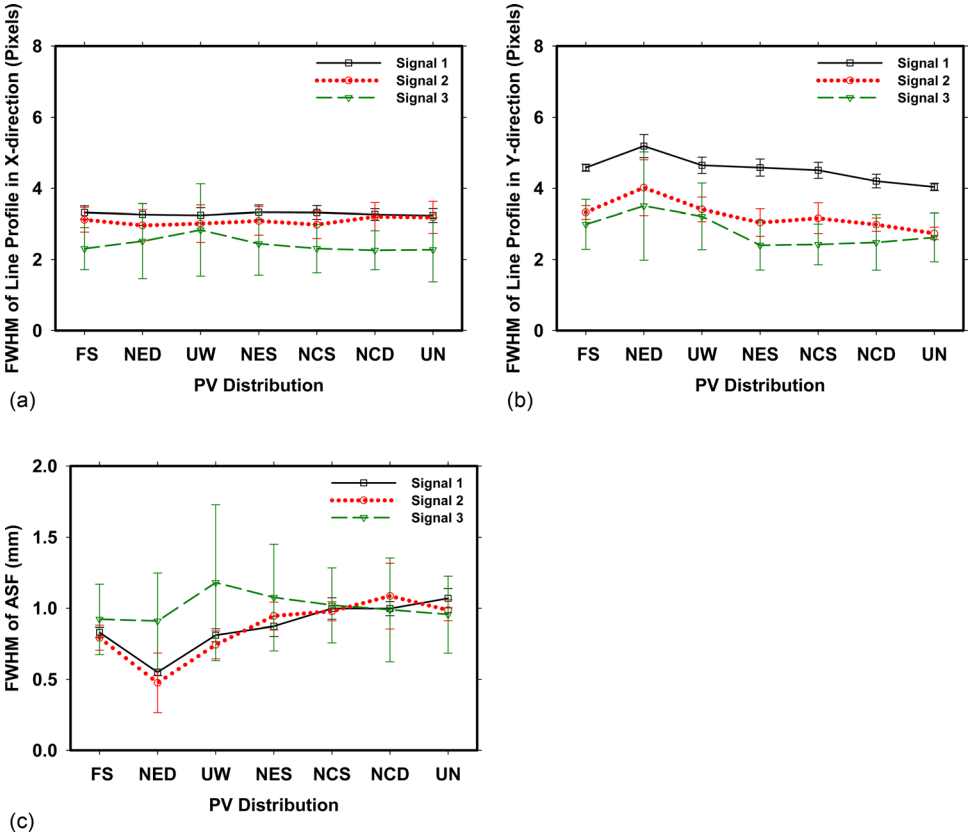

FIG. 5. Comparison of image blurring in three directions for the different PV distributions. The FWHMs of the line profiles in the (a) X-direction and (b) Y-direction on the X-Y focal planes and the FWHMs of the ASF in the (c) Z-direction for three clusters of simulated calcifications selected from the ACR phantom images reconstructed by SART with selective diffusion regularization are compared. The side length of one pixel is 0.1 mm. All values of signal 1 and signal 2 were obtained by averaging six repeated measurements. All values of signal 3 were obtained by averaging five simulated microcalcifications in the speck group of nominal size 0.24 mm and six repeated measurements. The error bars indicate one standard deviation of the measurements. Six subsets and the full set of projection views are compared.

III.B. Microcalcifications in breast

The DBT scans of three human subjects containing microcalcifications with a range of sizes were chosen for analysis. Because there were no repeated measurements for human subject DBTs, the variations of the single measurements were large. Only the results for a relatively large calcification in each case are shown. The ROIs on the in-focus DBT slice of the chosen calcification for the three subjects are shown in Figs. 6(a)–6(c).

The CNRs of the three microcalcifications are plotted in Fig. 7. For all three microcalcifications, the CNRs obtained from the six PV distributions were comparable and inferior to that obtained from the full set PV distribution, which was similar to the observation from signal 1 (relatively large one) in the ACR phantom. For other subtle microcalcifications (graphs not shown), the CNRs did not present any consistent trend due to the large statistical uncertainty, which confirmed what we observed for the ACR phantom if we compared only one single measurement.

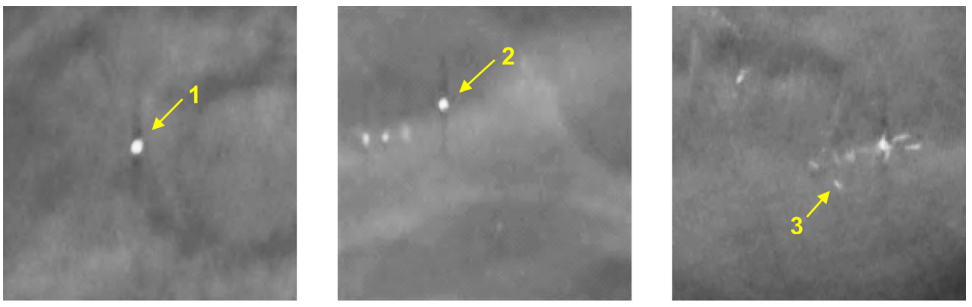

FIG. 6. Regions of interest from the in-focus DBT slices intersecting a microcalcification in three human subjects selected for analysis in this study. The DBT slices were reconstructed from 21 PVs by SART with selective diffusion regularization.

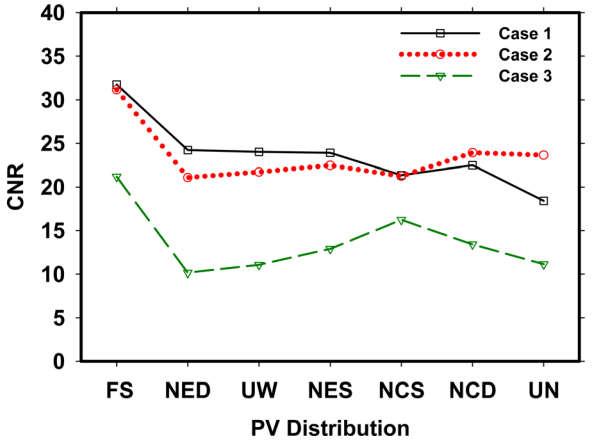

FIG. 7. Comparison of the CNR using different PV distributions. The CNR of relatively large microcalcifications selected from DBT scans of three human subjects reconstructed by SART with selective diffusion regularization are compared.

The image blurring in the three directions using different PV distributions are compared in Figs. 8(a)–8(c). In the X-direction, the variations of the FWHMs obtained from the different PV distributions were well within one pixel. In the Y-direction, the trends of the three signals were consistent with those observed from the ACR phantom data. Most PVs in NED were located at large angles; whereas, most PVs in UN were located at small angles; resulting in greater blurring for the former than the latter. For the interplane artifacts in the Z-direction, the trends for all three microcalcifications were similar to those observed for the large microcalcifications in the ACR phantom. The FWHMs for PV distributions with more PVs at large angles were 0.5 to 1 mm smaller than the FWHMs for distributions with more PVs at small angles. For small, subtle microcalcifications in human subjects (graphs not shown), the variations in the FWHMs were too large and no trend could be observed.

IV. DISCUSSION

In this study, we investigated the effect of the PV distribution in DBT on CNR and spatial blurring of microcalcifications within the tomosynthesized slices (X-Y plane) and in the depth (Z) direction. Our preliminary results demonstrate that for microcalcifications, PV distributions have a strong impact on the interplane blurring in the Z-direction and affect the in-plane blurring in the x-ray source motion direction. The interplane blurring decreased as the acquisition angular range increased. In the case of equal angular range, the PV distribution with a larger number of PVs at large projection angles resulted in better interplane resolution. In the x-ray source motion direction, the in-plane blurring increased as the acquisition angular range increased. In the case of equal angular range, the distribution with more PVs at small projection angles resulted in better in-plane resolution. However, the in-plane sharpness of calcifications in the direction perpendicular to the x-ray source motion direction

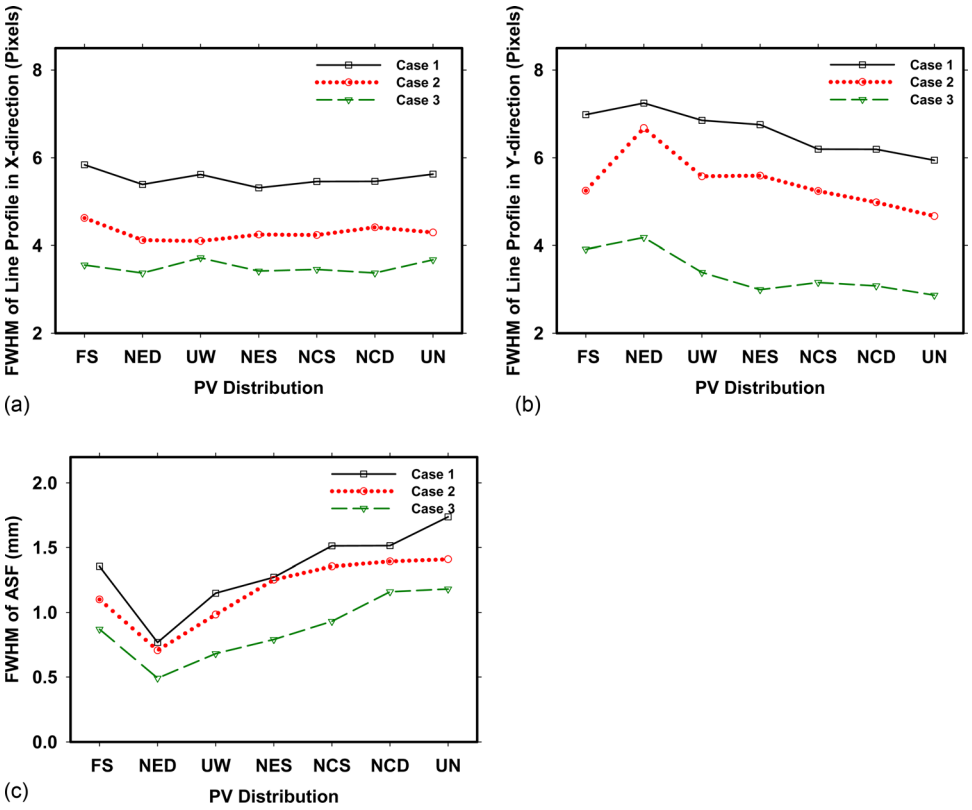

FIG. 8. Comparison of image blurring in three directions for the different PV distributions. The FWHMs of the line profiles in the (a) X-direction and (b) Y-direction on the X-Y focal planes and the FWHMs of the ASF in the (c) Z-direction for three relatively large microcalcifications selected from DBT of three human subjects reconstructed by SART with selective diffusion regularization are compared. The pixel size is 0.1 mm × 0.1 mm.

did not show strong dependence on the PV distributions evaluated in this study.

The effect of the PV distributions on spatial blurring depends on calcification size. The trends were better observed from the analysis of phantom calcifications, for which repeated measurements of the same calcifications under the same imaging conditions were possible. The average over repeated measurements reduced the statistical variations and provided an estimation of the standard deviations. The standard deviation was small for relatively large signals and very large for small signals. In the X-direction (perpendicular to the x-ray source motion direction), the projection geometry has negligible effect on image blurring, as can be seen from the FWHMs of the line profiles for large calcifications, which were almost constant within the measurement errors. For small calcifications, the average FWHMs varied for the different PV distributions but the variations were still within the standard deviations of the measurements.

Our observations on spatial blurring of microcalcifications are consistent with theoretical analysis of image blurring effect of DBT systems. Previous theoretical analysis of image blurring in the Z-direction in terms of slice sensitivity profile[7] or depth of field[10] showed that image blurring is inversely proportional to the scan angle. We observed a similar trend of image blurring in the Z-direction in terms of FWHM in the current study using both phantom and human subject data.

The effect of PV distributions on CNR of microcalcifications observed in our study was also similar to that obtained from computer simulation for relatively high-contrast microcalcifications.[12] The simulated microcalcification by Sechopoulous *et al*. was a cube of side-lengths of 0.4 mm, which was between the microcalcification specks of nominal sizes 0.54 and 0.32 mm in the ACR phantom or signal 1 and signal 2 chosen in our study. Sechopoulos *et al*. concluded that CNR of microcalcifications was less sensitive to angular range, which was consistent with our results for the relatively high-contrast microcalcifications. In their study, the accuracy of the CNR measurement of microcalcifications was limited by image noise, which was alleviated by the selective-diffusion regularization used in our SART reconstruction.

Our SD regularization method for DBT reconstruction smoothed the background noise and preserved the sharpness of potential microcalcifications, thereby improving the CNR as demonstrated in our previous study.[17] The less noisy background provided more reliable baselines for fitting the Gaussian functions to the profiles of the calcifications during the FWHM measurements. The degree of regularization could be adjusted by the regularization parameters, which we kept to be the same as those determined previously[17] for all PV distributions to reduce the number of variables. The current study focused on the comparison of the PV distributions while the reconstruction method was fixed. Further study is underway to compare reconstruction techniques for different applications.

We selected six subsets of PV distributions within the 21 PVs in the original DBT scans under the constraint of constant total dose (11 PVs). Because of the already fixed image acquisition angles, the different PV distribution that can be subsampled from the original 21 PVs are limited. This limitation was more apparent for the nonuniform central category; the difference between the NCD and NCS distributions was small, as also confirmed by the image quality measures (Figs. 4 and 5). Study of a wider range of combinations of angular acquisition parameters and PV distributions would require a computer simulation model or a DBT system with variable settings for PV acquisition.

For detection of calcifications by radiologists using present criteria developed with single projection mammograms, the better interplane resolution obtained from a larger angular range or, for an equal angular range, with a larger fraction of PVs at large projection angles may not be very essential. The reversal of these trends for in-plane blurring in the x-ray source motion direction and the slight trend, for subtle microcalcifications, toward higher CNR for PV distributions with dense PVs at small angles suggests that, for calcifications, a central weighting of projection angles may prove worthwhile. However, the distortion of the shape and size of the microcalcifications by the interplane artifacts could be a concern as linear and branching calcifications have higher likelihood of being malignant. As more experience is gained with DBT, less interplane blurring may also prove significant for visualization of the distribution of calcifications in the third dimension in relation to other breast structures such as ducts and vessels, which may provide important diagnostic information. For much larger features including soft tissue lesions and fibroglandular structures, the improvement of the ASF with a large angular range or peripherally weighted PV distributions will be more important, as demonstrated in our previous study.[9] The trade-offs between the image quality of different types of lesions should be taken into consideration in the design of a DBT system. One can envision that a DBT system with variable PV distribution settings may be developed so that a proper PV distribution may be chosen during diagnostic workup when a specific type of lesion is suspected or certain lesion characteristics are of interest. Further observer or clinical studies of the effects of the DBT parameters on detection and characterization of different types of breast lesions are warranted.

V. CONCLUSION

We studied the effect of different PV distributions on image quality of microcalcifications in DBT reconstruction using SART. Six different subsets of PVs were selected from the acquired PVs to simulate DBTs with different angular ranges and uniform or nonuniform angular increments. The FWHMs of line profiles in the X-Y focal plane and the FWHMs of ASFs in the depth direction were quantitatively analyzed for measuring the image blurring caused by different PV distributions. The results demonstrated that the PV distributions affect the image quality of microcalcifications in DBT. The relative importance of the impact depends on the characteristics of the signal and the direction relative to

the tomographic scan. For a given number of PVs, the angular range and the distribution of the PVs affect the degree of in-plane and interplane blurring in opposite ways. The design of the scan parameters of tomosynthesis systems would require proper consideration of the characteristics of the signals of interest and the potential trade-off of the image quality of different types of signals.

ACKNOWLEDGMENTS

This work is supported by USPHS grants R33 CA120234, RO1 CA91713, and RO1 CA151443. The digital breast tomosynthesis system was developed by the GE Global Research Group, with input and some revisions from the University of Michigan investigators, through the Biomedical Research Partnership (USPHS grant CA91713, PI: Paul Carson, Ph.D.). The content of this paper does not necessarily reflect the position of the funding agencies and no official endorsement of any equipment and product of any companies mentioned should be inferred.

[a]Author to whom correspondence should be addressed. Electronic mail: yaol@med.umich.edu; Telephone: (734) 647-8556; Fax: (734) 615-5513.

[1]L. T. Niklason *et al.*, "Digital tomosynthesis in breast imaging," Radiology **205**, 399–406 (1997).
[2]T. Wu *et al.*, "Tomographic mammography using a limited number of low-dose cone-beam projection images," Med. Phys. **30**, 365–380 (2003).
[3]S. P. Poplack, T. D. Tosteson, C. A. Kogel, and H. M. Nagy, "Digital breast tomosynthesis: Initial experience in 98 women with abnormal digital screening mammography," Am. J. Roentgenol. **189**, 616–623 (2007).
[4]D. Gur, G. S. Abrams, D. M. Chough, M. A. Ganott, C. M. Hakim, R. L. Perrin, G. Y. Rathfon, J. H. Sumkin, M. L. Zuley, and A. I. Bandos, "Digital breast tomosynthesis: Observer performance study," Am. J. Roentgenol. **193**, 586–591 (2009).
[5]H. J. Teertstra, C. E. Loo, M. A. A. J. van den Bosch, H. van Tinteren, E. J. T. Rutgers, S. H. Muller, and K. G. A. Gilhuijs, "Breast tomosynthesis in clinical practice: Initial results," Eur. Radiol. **20**, 16–24 (2010).
[6]A. R. Pineda, S. Yoon, D. S. Paik, and R. Fahrig, "Optimization of a tomosynthesis system for the detection of lung nodules," Med. Phys. **33**, 1372–1379 (2006).
[7]B. J. Li, G. B. Avinash, J. W. Eberhard, and B. E. H. Claus, "Optimization of slice sensitivity profile for radiographic tomosynthesis," Med. Phys. **34**, 2907–2916 (2007).
[8]Y. H. Hu, B. Zhao, and W. Zhao, "Image artifacts in digital breast tomosynthesis: Investigation of the effects of system geometry and reconstruction parameters using a linear system approach," Med. Phys. **35**, 5242–5252 (2008).
[9]Y. Zhang, H. P. Chan, M. M. Goodsitt, A. Schmitz, J. Eberhard, and B. Claus, "Investigation of different PV distributions in digital tomosynthesis mammography (DTM)," *Proceedings of the 9th International Workshop on Digital Mammography* IWDM-2008, (2008), pp. 593–600.
[10]B. Ren, C. Ruth, Y. Zhang, A. Smith, C. Williams, B. Polischuk, and Z. Jing, "The CNR method in scan angle optimization of tomosynthesis and its limitations," SPIE Med. Imag. Conf. – Phys. Med. Imag., **7258**, 1–10 (2009).
[11]A. S. Chawla, J. Y. Lo, J. A. Baker, and E. Samei, "Optimized image acquisition for breast tomosynthesis in projection and reconstruction space," Med. Phys. **36**, 4859–4869 (2009).
[12]I. Sechopoulos and C. Ghetti, "Optimization of the acquisition geometry in digital tomosynthesis of the breast," Med. Phys. **36**, 1199–1207 (2009).
[13]I. Reiser and R. M. Nishikawa, "Task-based assessment of breast tomosynthesis: Effect of acquisition parameters and quantum noise," Med. Phys. **37**, 1591–1600 (2010).
[14]R. M. Nishikawa, I. Reiser, and P. Seifi, "A new approach to digital breast tomosynthesis for breast cancer screening," Proc. SPIE Med. Imag. 6510, 3C1–3C8 (2007).
[15]T. Wu, R. H. Moore, E. A. Rafferty, and D. B. Kopans, "A comparison of reconstruction algorithms for breast tomosynthesis," Med. Phys. **31**, 2636–2647 (2004).
[16]Y. Zhang, H.-P. Chan, B. Sahiner, J. Wei, M. M. Goodsitt, L. M. Hadjiiski, J. Ge, and C. Zhou, "A comparative study of limited-angle cone-beam reconstruction methods for breast tomosynthesis," Med. Phys. **33**, 3781–3795 (2006).
[17]Y. Lu, H. P. Chan, J. Wei, and L. M. Hadjiiski, "Selective-diffusion regularization for enhancement of microcalcifications in digital breast tomosynthesis reconstruction," Med. Phys. **37**, 6003–6014 (2010).
[18]R. L. Siddon, "Fast calculation of the exact radiological path for a three-dimensional CT array," Med. Phys. **12**, 252–255 (1985).
[19]M. Jiang and G. Wang, "Convergence of the simultaneous algebraic reconstruction technique (SART)," IEEE Trans. Image Proc. **12**, 957–961 (2003).
[20]C. Riddell, H. Benali, and I. Buvat, "Diffusion regularization for iterative reconstruction in emission tomography," IEEE Trans. Nucl. Sci. **51**, 712–718 (2004).